

# Non-trivial topological surface states regulation of 1 T-OsCoTe<sub>2</sub> enables selective C–C coupling for highly efficient photochemical CO<sub>2</sub> reduction toward C<sub>2+</sub> hydrocarbons

Kangwang Wang <sup>a,1</sup>, Mingjie Wu <sup>b,1</sup>, Peifeng Yu <sup>a</sup>, Hector F. Garces <sup>c</sup>, Ying Liang <sup>d</sup>, Longfu Li <sup>a</sup>, Lingyong Zeng <sup>a</sup>, Kuan Li <sup>a</sup>, Chao Zhang <sup>a</sup>, Kai Yan <sup>e,\*</sup>, Huixia Luo <sup>a,\*</sup>

<sup>a</sup> School of Materials Science and Engineering, State Key Laboratory of Optoelectronic Materials and Technologies, Guangdong Provincial Key Laboratory of Magnetoelectric Physics and Devices, Key Lab of Polymer Composite & Functional Materials, Sun Yat-sen University, Guangzhou 510275, China

<sup>b</sup> State Key Laboratory of New Textile Materials and Advanced Processing Technologies, Wuhan Textile University, Wuhan 430200, China

<sup>c</sup> School of Engineering, Brown University, 182 Hope Street, Providence, USA

<sup>d</sup> The Basic Course Department, Guangzhou Maritime University, Guangzhou 510800, China

<sup>e</sup> School of Environmental Science and Engineering, Sun Yat-sen University, Guangzhou 510275, China



## ARTICLE INFO

### Keywords:

Topological surface states  
Electronic properties  
CO<sub>2</sub> conversion  
C<sub>2+</sub> hydrocarbons  
C–C coupling

## ABSTRACT

Despite ongoing research, the rational design of non-trivial topological semimetal surface states for the selective photocatalytic CO<sub>2</sub> conversion into valuable products remains full of challenges. Herein, we present the synthesis of lattice-matched 1 T-OsCoTe<sub>2</sub> for the photoreduction upgrading of CO<sub>2</sub> to tri-carbon (C<sub>3</sub>) alkane (propane, C<sub>3</sub>H<sub>8</sub>) by the integration of experimental work and theory prediction/calculation. Experimental studies suggested a high electron-based selectivity of 71.2 % for C<sub>3</sub>H<sub>8</sub> and an internal quantum efficiency of 54.6 % at 380 nm. In-situ X-ray photoelectron spectroscopy and X-ray absorption fine structure spectroscopy demonstrated that Co and Os atoms coordinated with Te atoms enable an efficient Os–Te–Co electron transfer to activate the generation of \*CH<sub>3</sub>, \*CHOCO and \*CH<sub>2</sub>OOCOCO. Density functional theory calculations further confirmed Os–Te–Co electron bridging on the improved CO<sub>2</sub> conversion kinetics. To our knowledge, this is the first report suggesting the role of Os atoms in accelerating the photocatalytic CO<sub>2</sub> conversion activity of the topological semimetal 1 T-OsCoTe<sub>2</sub>.

## 1. Introduction

The surface states of catalysts, in which charge transport and reactant conversion occur simultaneously, plays a central role compared to the bulk state in determining its catalytic performance [1,2]. However, the surface states of catalysts are easily affected and disrupted by the adsorption and desorption of intermediates, fluctuations of surface defects, and potential changes during photoelectrochemical reactions. As time goes on, this dilemma can be skillfully resolved via establishing non-trivial topological surface states (TSSs), which are energy band structures protected by the bulk symmetry. Under this unique protection, the TSSs are unaffected by surface modifications and multiphase catalytic defects, enhancing the activity and stability of the catalysts [3, 4]. Moreover, the energy dispersion relation of the non-trivial TSSs

results in extremely high carrier mobility and an exotic partial density of states (PDOS), which is crucial for promoting fast catalytic reactions [5, 6].

1 T-CoTe<sub>2</sub>, a typical type-II Dirac semimetal of transition metal-sulfide compounds, has been at the frontier of electrocatalytic research due to its diverse phase structure and ultrahigh carrier mobility [7,8]. More specifically, Co<sup>2+</sup> sites play a crucial role in improving the selectivity of multi-carbon (C<sub>2+</sub>) hydrocarbons, which can not only accelerate the adsorption of \*CO and promote the C–C coupling reaction but also stabilize the critical intermediates for generation of C<sub>2+</sub> hydrocarbons [9,10]. Unfortunately, it remains a challenge for achieving satisfied products selectivity and internal quantum efficiency (IQE) due to the complex multiple-electron reduction in the CO<sub>2</sub> reduction reaction (CO<sub>2</sub>RR) process. The introduction of another doping metal is an

\* Corresponding authors.

E-mail addresses: [yank9@mail.sysu.edu.cn](mailto:yank9@mail.sysu.edu.cn) (K. Yan), [luohx7@mail.sysu.edu.cn](mailto:luohx7@mail.sysu.edu.cn) (H. Luo).

<sup>1</sup> These authors contributed equally

effective way to regulate and improve the stability of  $\text{Co}^{2+}$ , while the difference in atomic radii between the heteroatom and the Co atom causes lattice distortion, which affects the *d*-band center of the catalyst and thus changes the binding ability of the reaction intermediates on the catalyst surface [11]. More importantly, the doping metal also affects the activity of the competitive hydrogen evolution reaction (HER) [12]. Therefore, modulation of \*CO binding energy and suppression of HER are essential objectives in developing metal-atom doped Co-based catalysts.

Based on the considerations mentioned above, integrating the advantages of a topological semimetal ( $1\text{-T-CoTe}_2$ ) unit with robust surface states and a normal semiconductor ( $2\text{-H-OsTe}_2$ ) unit into one alliance would be of great interest to optimize their potential for high-performance  $\text{CO}_2\text{RR}$ . In this paper, for the first time, we present a detailed investigation of the electronic structure and catalytic mechanism of  $1\text{-T-OsCoTe}_2$  via combining first-principles calculations with *in-situ* X-ray photoelectron spectroscopy (XPS) and X-ray absorption fine structure spectroscopy (XAFS) experiments. The investigations demonstrate that the synergy between Co and Os metal sites is crucial for enhanced photocatalytic  $\text{CO}_2\text{RR}$  performance. Specifically, Co atoms act as the active catalytic sites, while adjacent Os atoms serve as promoters, and Te atoms function as the transport bridge facilitating electron flow. Density functional theory (DFT) calculations corroborate the strong orbital coupling between Os and Co atoms, causing the *d*-band structure with improved photoactivity. *In-situ* diffuse reflectance-infrared Fourier-transform spectroscopy (DRIFTS) combined with theory calculations reveal that the synergistic effect of Os and Co metal sites as well their Te electron bridging not only reduces the reaction barrier for the formation of \*CHOCO and \*CH<sub>2</sub>OOCOCO, but also retards undesired HER, synergistically boosting  $\text{CO}_2$  conversion to propane (tri-carbon ( $\text{C}_3$ ) alkane,  $\text{C}_3\text{H}_8$ ).

## 2. Experiment section

### 2.1. Materials and reagents

Tellurium powder (Te, more than 200 mesh) was purchased from Shanghai Aladdin Biochemical Technology Co., Ltd. Cobalt powder (Co, 99.99 %) and Osmium powder (Os, 99.99 %) were used without further purification. 5,5'-dimethyl-1-pyrroline N-oxide (DMPO) furnished by Shantou Xilong Chemical Co., Ltd. in China was used to trap the generated \*CH<sub>3</sub> or \*OH radicals in the reaction. All of the reagents used in our experiments have analytical grade purity and were used without further purification. De-ionized water ( $\text{H}_2\text{O}$ ) was obtained from a Millipore system.

### 2.2. Preparation of $1\text{-T-OsCoTe}_2$ and $2\text{-H-OsCoTe}_2$

To synthesize polycrystalline samples of  $1\text{-T-OsCoTe}_2$  and  $2\text{-H-OsCoTe}_2$ , stoichiometric amounts of the constituent elements were weighted and grounded with mortar and pestle under inert atmosphere (glovebox). The reaction mixtures were then loaded into quartz tubes and subsequently sealed under vacuum ( $10^{-3}$  mbar). The synthesis of  $1\text{-T-OsCoTe}_2$  was performed via heating the evacuated quartz tubes at 1000 °C for 4 h with a heating rate of 5 °C·min<sup>-1</sup>, subsequently the temperature was decrease to 800 °C at 5 °C·min<sup>-1</sup> and kept for 24 h. Finally, the mixtures were cooled to room temperature at 0.5 °C·min<sup>-1</sup>.  $2\text{-H-OsCoTe}_2$  was synthesized by slowly heating the ampoule with the reaction mixture to 1000 °C, keeping it at 1000 °C for 5 days, and cooling the ampule slowly to room temperature over 1 day. In order to ensure the homogeneity of the samples, the obtained mixtures were reground and heated again at 1000 °C for 4 days. After cooling to room temperature,  $2\text{-H-OsCoTe}_2$  was obtained.

The  $1\text{-T-CoTe}_2$  and  $2\text{-H-CoTe}_2$  were prepared following the above synthesis steps of  $1\text{-T-OsCoTe}_2$  and  $2\text{-H-OsCoTe}_2$  without adding Os powder. The  $2\text{-H-OsTe}_2$  was prepared following the above synthesis

steps of  $2\text{-H-OsCoTe}_2$  without adding Co powder. It is worth to mention here that, to gain deeper insight of Te electron bridging characteristics, the pure OsCo alloys were prepared following the above synthesis steps of  $1\text{-T-OsCoTe}_2$  without adding Te powder.

### 2.3. Photocatalytic $\text{CO}_2\text{RR}$ measurements

Photocatalytic  $\text{CO}_2\text{RR}$  measurement was conducted in an online trace gas analysis system with a gas chromatography-mass spectrometry (GC-MS, Agilent GC/MS-7000D) and <sup>1</sup>H nuclear magnetic resonance (<sup>1</sup>H NMR) spectroscopy. Firstly, 50 mg of photocatalyst and 100 mL of aqueous acetonitrile (MeCN) solution [13] were added in the Pyrex glass reaction cell with sonication. Then, the reactor system was then filled with pure  $\text{CO}_2$  gas (80 kPa) following complete evacuation. After adsorption equilibrium, the reactor system was put under a simulated light source which was provided by a 300 W Xe lamp (Beijing Perfect-light, Microsolar 300, 100 mW cm<sup>-2</sup>) with a UVCUT-420 nm filter to cut-off the light with wavelengths lower than 420 nm (i.e.  $\lambda > 420$  nm), and the chilled water controlled the system temperature. Finally, the gas and liquid produced were analyzed every 1 h through GC-MS and <sup>1</sup>H NMR spectroscopy (Bruker AVIII HD 600), respectively. Notably, for the <sup>1</sup>H NMR measurement, 0.5 mL of the product solution was mixed with 0.1 mL of  $\text{D}_2\text{O}$  and 10  $\mu\text{L}$  of dimethylsulfoxide (DMSO, as the internal standard). In addition, all the experiments were repeated at least 3 times in parallel to obtain an average value and error bars indicate standard deviations.

### 2.4. Characterization

Powder X-ray diffraction (PXRD) patterns were collected on an X-ray diffractometer (X' Pert3 Powder) equipped with a Kratky block-collimation system at  $25.0 \pm 0.1$  °C and a sealed-tube X-ray generator with the Cu target operating at 45 kV and 40 mA. Inductively coupled plasma optical emission spectrometer (ICP-OES) was tested on an Agilent 7500cx instrument with an attached laser ablation system. UV-Vis-NIR diffused reflectance spectra (DRS) was collected on a spectrophotometer (UV-3100, Shimadzu, Japan) with  $\text{BaSO}_4$  as the background holder. Steady-state photoluminescence (PL) and time-resolved PL (TRPL) measurements were performed on a Hamamatsu instrument (Hamamatsu C5680, Japan), with an excitation wavelength of 320 nm.  $\text{CO}_2$  adsorption isotherms were obtained at 25 °C via using a Quantachrome Autosorb-iQ adsorption analyzer after the degassing process at 200 °C for 12 h.

### 2.5. Computational method of charge distribution

All of the calculations are performed in the framework of the spin-polarized density functional theory with the projector augmented plane-wave method, as implemented in the Materials Studio 2019 and Vienna ab initio simulation package (VASP) [14]. The generalized gradient approximation (GGA) proposed by Perdew, Burke, and Ernzerhof is selected for the exchange-correlation potential [15,16]. The van der Waals interaction was taken into account using DFT-D3 method with Becke-Jonson damping dispersion correction [17,18]. The cut-off energy for plane wave was set to 400 eV. The energy criterion was set to  $10^{-5}$  eV in iterative solution of the Kohn-Sham equation. The Brillouin-zone sampling was conducted using Monkhorst-Pack (MP) grids of special points with the separation of 0.04 Å<sup>-1</sup>. All the structures are relaxed until the residual forces on the atoms have declined to less than 0.02 eV Å<sup>-1</sup>. A Gaussian smearing of 0.05 eV was applied to speed up self-consistent field iteration. Data analysis and visualization are carried out with the help of VASPKIT, Materials Studio 2019, and VESTA. DFT + *U* approach [19] with *U* = 3.3 eV was considered to evaluate the influence of strongly correlated *d* electrons of Co and Os on the calculated free energies. Adsorption energy ([ads]) was defined as  $E_{[\text{ads}]} = E_{[\text{adsorbate}/\text{substrate}]} - E_{[\text{substrate}]} - E_{[\text{adsorbate}]}$ , where  $E_{[\text{substrate}]}$  is

the total energy of substrate,  $E_{[\text{adsorbate}/\text{substrate}]}$  is the total energy when carbon monoxide (CO), methane (CH<sub>4</sub>), ethylene (C<sub>2</sub>H<sub>4</sub>) or C<sub>3</sub>H<sub>8</sub> is adsorbed on the substrate surface,  $E_{[\text{adsorbate}]}$  refers to the energy of CO, CH<sub>4</sub>, C<sub>2</sub>H<sub>4</sub> or C<sub>3</sub>H<sub>8</sub>. The Gibbs free energy change ( $\Delta G$ ) was defined as  $\Delta G = \Delta E + \Delta E_{ZPE} - T\Delta S$ , where  $\Delta E$  is the energy difference between the reactants and product obtained through DFT calculations.  $\Delta E_{ZPE}$  and  $\Delta S$  are the changes in the zero-point energies (ZPE) and entropy.  $T$  represents the temperature and was set as 298.15 K.

### 3. Result and discussion

#### 3.1. Structural characterization

Based on transmission electron microscopy (TEM) image, 1 T-OsCoTe<sub>2</sub> demonstrates a typical bulk-like structure and possesses abundant pores (Fig. 1a). Notably, energy-dispersive X-ray spectroscopy (EDS) mapping indicates that Co elements on 1 T-OsCoTe<sub>2</sub> are distributed around Os elements, and there are high-density bright spots on Te elements, implying atomically dispersed Co and Os species (Fig. 1b). Meanwhile, high-resolution TEM (HRTEM) image shows that the lattice spacings of 3.64 and 1.93 Å (Fig. 1e) correspond to (111) plane of 1 T-CoTe<sub>2</sub> and (311) plane of 2 H-OsTe<sub>2</sub>, respectively (Fig. 1c). From the results, the phases of 1 T-CoTe<sub>2</sub> and 2 H-OsTe<sub>2</sub> belong to P-3m1 and Pa-3 space groups, respectively. This intuitive result provides direct evidence for successfully constructing 2 H-OsTe<sub>2</sub> and 1 T-CoTe<sub>2</sub> composite structures. To further confirm, an aberration-corrected high-angle annular dark-field scanning TEM (AC HAADF-STEM) image is employed and displayed two kinds of points with different brightness and colors through pseudo-color transformation (Fig. 1f and g). The HAADF-STEM

image of 1 T-OsCoTe<sub>2</sub> reveals a crystal structure resembling that of 1 T-CoTe<sub>2</sub> (P-3m1) and 2 H-OsTe<sub>2</sub> (Pa-3) (Fig. S1), with no discernible Os crystalline phase observed, potentially attributable to the low and uniform distribution of Os species (Fig. 1g). By comparing the magnified HAADF-STEM images, they match well with the lattice models after XRD optimization (Fig. S2). Selected regional electron diffraction (SAED) pattern shows diffraction rings and spots, suggesting polycrystalline and monocrystalline composite properties of 1 T-OsCoTe<sub>2</sub> (Fig. 1h). As an overall picture, the chemical composition of 1 T-OsCoTe<sub>2</sub> is quantitatively determined by ICP-OES results (Fig. S3a), which is similar to the chemical formula of 1 T-OsCoTe<sub>2</sub>. Meanwhile, diffraction rings of 2 H-OsCoTe<sub>2</sub> can be observed in the SAED pattern, representing the polycrystalline property of 2 H-OsCoTe<sub>2</sub> (Fig. 1d and S3b–e).

#### 3.2. Electronic structure analysis

The electronic structure information of 1 T-OsCoTe<sub>2</sub> and 2 H-OsCoTe<sub>2</sub> were compared via in-situ XPS spectra (Fig. 2 and S4). After 20 min of illumination, the binding energy of Co 2p shifts to the right via 1.97 eV, and then returns to the “dark-state” after 10 min of light-off, suggesting electronic gain of 1 T-CoTe<sub>2</sub> upon light illumination (Fig. 2a). This is mainly due to the electrons in the conduction band of 2 H-OsTe<sub>2</sub> being transferred to Co 2p orbitals on 1 T-CoTe<sub>2</sub> through a built-in electric field force [20,21], and the binding energy change of Os 4f on 2 H-OsTe<sub>2</sub> further confirms the direction of electron migration (Fig. 2b). Theoretically, the binding energy shift of Te 3d should be opposite to that of Os 4f on 2 H-OsTe<sub>2</sub>. Nevertheless, this is not the case, and the binding energy of Te 3d shifts to the right by 3.02 eV after 20 min of light-on, and then to the left via 1.47 eV after 40 min of

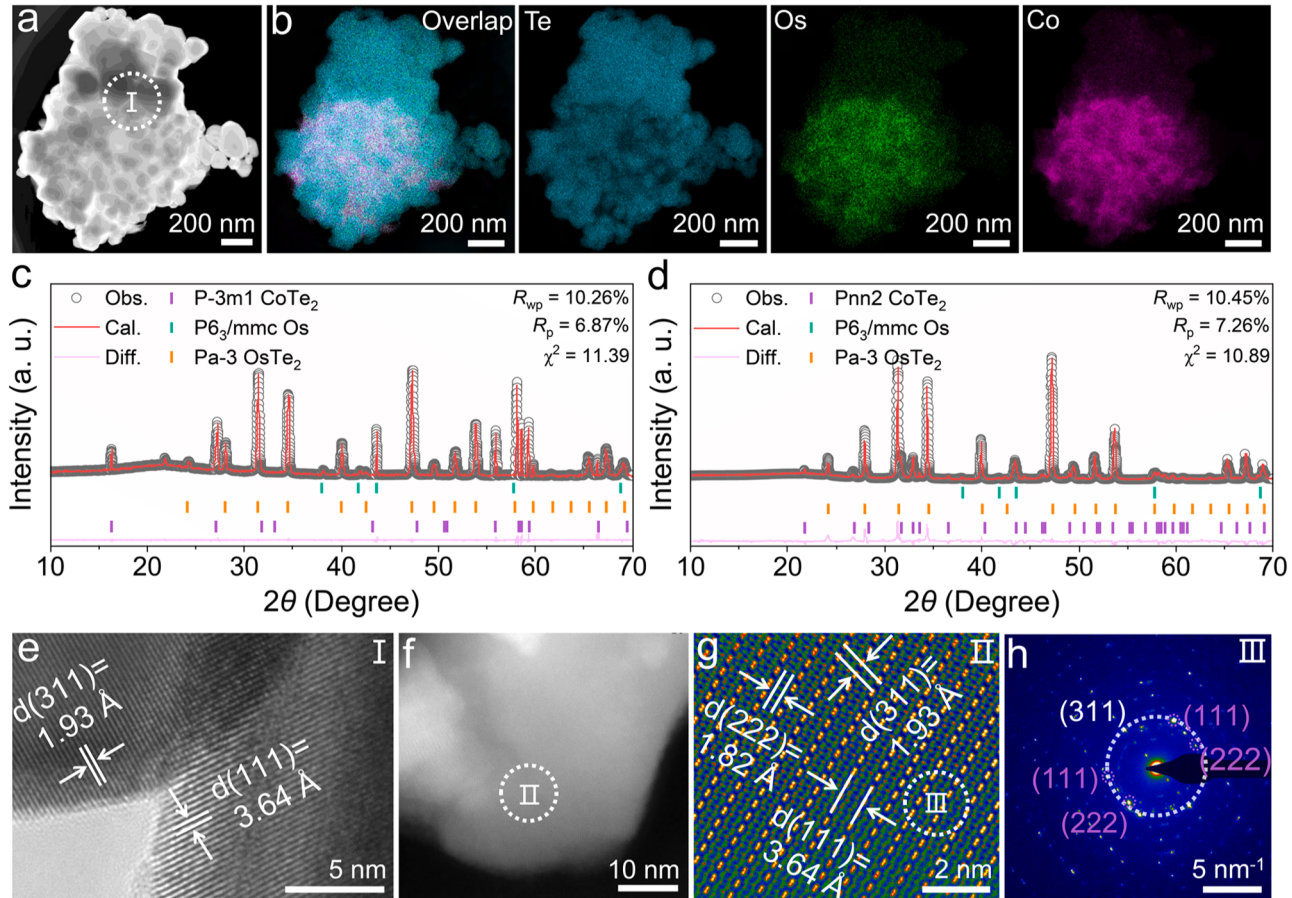


**Fig. 1.** (a) TEM and (b) EDS elemental mapping of 1 T-OsCoTe<sub>2</sub>, respectively. XRD profiles and Rietveld refinement results of (c) 1 T-OsCoTe<sub>2</sub> and (d) 2 H-OsCoTe<sub>2</sub>, respectively. (e) HRTEM image of 1 T-OsCoTe<sub>2</sub>. (f,g) HAADF-STEM images and (h) SAED pattern of 1 T-OsCoTe<sub>2</sub>, respectively.

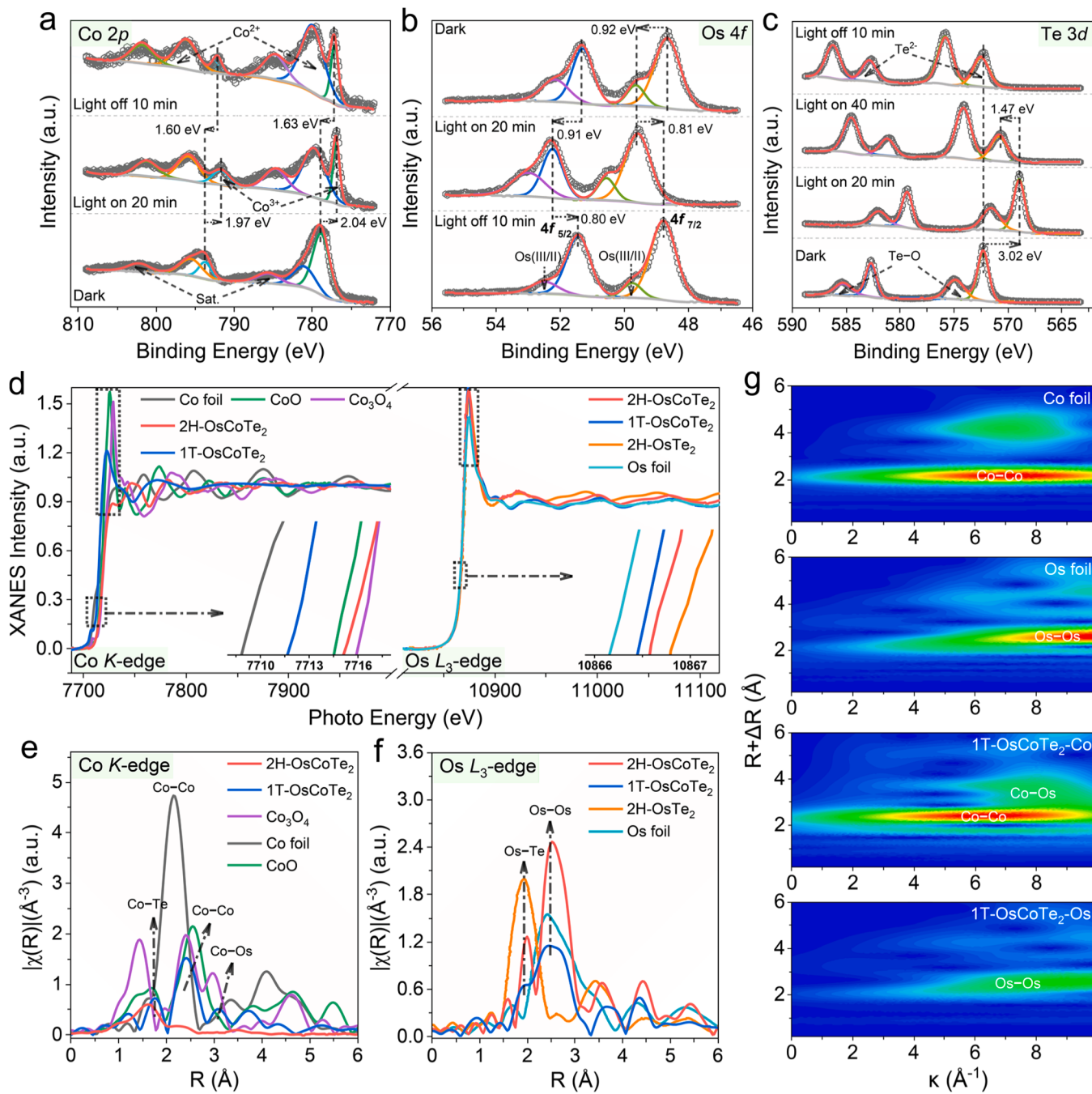


**Fig. 2.** In-situ XPS (a) Co 2p, (b) Os 4f, and (c) Te 3d spectra of 1 T-OsCoTe<sub>2</sub>. (d) Co K-edge and Os L<sub>3</sub>-edge XANES spectra of different samples. (e) Co K-edge and (f) Os L<sub>3</sub>-edge EXAFS in R-space. (g) WT spectra for the  $\kappa^3$ -weighted  $\chi(\kappa)$  K-edge EXAFS signals of Co foil, Os foil, Co K-edge, and Os L<sub>3</sub>-edge of 1 T-OsCoTe<sub>2</sub>.

light-on. In sharp contrast, the binding energy of Te 3d does not completely return to the “dark-state” after 10 min of light-off (Fig. 2c) [22], which indicates that there are two electron transport processes in 1 T-OsCoTe<sub>2</sub> under light radiation. The first process is a direct electron transfer from Os atoms to Te atoms (i.e., causing a decrease in the binding energy of Te 3d). The second process is an indirect electron transfer from Te atoms to Co atoms driven by an interfacial electric field (i.e., leading to an increase in the binding energy of Te 3d). The binding energy core-level peak for Te 3d does not shift, confirming that the two processes are balanced. Interestingly, the small changes in Os 4f binding energy before and after illumination disclose that the first electron transport process is the dominant one. The bulk electronic band structures and PDOS of 1 T-OsCoTe<sub>2</sub>, 2 H-OsCoTe<sub>2</sub>, 1 T-CoTe<sub>2</sub>, and 2 H-CoTe<sub>2</sub> without spin-orbit coupling (SOC) were calculated as shown

in Fig S5 and S6. The few crossings and low PDOS at the Fermi level ( $E_F$ ) of 1 T-CoTe<sub>2</sub> display its semimetallic properties. However, the PDOS at the Fermi surface in 1 T-OsCoTe<sub>2</sub> is clearly higher than that in 2 H-OsCoTe<sub>2</sub>, indicating faster charge transfer and lower resistance of 1 T-OsCoTe<sub>2</sub> than 2 H-OsCoTe<sub>2</sub>, which is in accordance with the transient photocurrents. In addition, the bulk electronic band structure (Fig S5a and b) denotes that the conduction and valence bands located near the  $E_F$  intersecting along G-L direction forms Dirac node, suggesting that 1 T-CoTe<sub>2</sub> possess ultra-high conductivity and mobility, which is a general feature of Dirac semimetal [6,7,23]. Thus, topologically protected surface states are accommodated at the 1 T-CoTe<sub>2</sub> (001) facet, which appear in the bandgap at the  $\Gamma$  point, as demonstrated in Fig S6a and c. Notably, the presence of TSSs was found in the surface energy bands of 1 T-CoTe<sub>2</sub> (001) with surface state energy levels near the  $E_F$

(~0.01 eV higher) (Fig S5b and e–i) [24], which means that non-trivial TSSs can provide additional electrons and facilitate the electrons transfer of Os–Te–Co electron bridging from the surface of 1 T-OsCoTe<sub>2</sub> to the adsorbed CO<sub>2</sub> molecules, which is conducive to CO<sub>2</sub>RR.

To systematically explore the active sites of the photocatalysts as well as the coordination environments of Os and Co atoms, XAFS spectroscopy was implemented for 1 T-OsCoTe<sub>2</sub> and 2 H-OsCoTe<sub>2</sub>. X-ray absorption near-edge structures (XANES) of Co K-edge indicate that the absorption edge of 2 H-OsCoTe<sub>2</sub> is located between CoO and Co<sub>3</sub>O<sub>4</sub>, meaning that the valence of Co element is between +2 and +3 [25]. The enlarged profile clarifies that the valence state of the Co element in 2 H-OsCoTe<sub>2</sub> is close to +2. Meanwhile, XANES spectra of Os L<sub>3</sub>-edge show that the positions of the absorption threshold of 1 T-OsCoTe<sub>2</sub> and 2 H-OsCoTe<sub>2</sub> are situated in Os foil and 2 H-OsTe<sub>2</sub> (Fig. 2c), which reveals that the valences of Os element are between 0 and +2 [26]. Extraordinarily, the intensity of the white-line peak of Co K-edge XANES spectrum of 1 T-OsCoTe<sub>2</sub> is lower than that of CoO, indicating a decrease in the PDOS and an increase in the electron filling of the d-band for the unoccupied state of Co 3d near the Fermi energy level. This result suggests that electrons are injected into the Co 3d orbitals after introducing 2 H-OsTe<sub>2</sub> [27,28]. Contrastingly, the white-line peak intensity of Os L<sub>3</sub>-edge XANES spectrum of 1 T-OsCoTe<sub>2</sub> is higher than that of 2 H-OsTe<sub>2</sub>. Moreover, the intensity of white-line peak and absorption edge of 1 T-OsCoTe<sub>2</sub> are significantly different from that of Os foil, while it is extremely close to that of 2 H-OsTe<sub>2</sub> (Fig. 2c), which suggests that the average Os valence state of 1 T-OsCoTe<sub>2</sub> is similar to that of 2 H-OsTe<sub>2</sub>, agreement with XPS results [26,29]. It is estimated that Co atoms sequentially form electron accumulation layers by swiping electrons from the surrounding Os atoms through Co–Te bonds. Significantly, the charge density around the Co atoms increases, further demonstrating the electron-donating nature of Os–Te bonds. As displayed by the PDOS in Fig. S6d and e, the higher electron density around the Co atoms modulates the 3d orbital structure, leading to a positive shift in the center of the d-band. The resulting electron-deficient Os atoms bring the whole 1 T-OsCoTe<sub>2</sub> close to a relatively high valence state, which can be further verified from the results of Os L<sub>3</sub>-edge k<sup>2</sup>-weighted oscillation (Fig. S6f). The first significant peak in EXAFS spectra of 1 T-OsCoTe<sub>2</sub> (Fig. 2d) denotes that Co atoms are coordinated with Te atoms nearest neighboring shell locates at ~1.76 Å, referring to the peak of Co–Te bonds in 1 T-CoTe<sub>2</sub> [30]. Simultaneously, the first significant peak can be attributed to Os–Te bonds that Os atoms are coordinated through Te atoms nearest neighboring shell at ~1.93 Å, which is well consistent with that of 2 H-OsTe<sub>2</sub>, indicating that Os atoms interact with Te atoms through Os–Te bonds (Fig. 2e). The detailed coordination environments of Co and Os atoms were further investigated by Fourier transform of extended X-ray absorption fine structures (EXAFS) and wavelet transforms (WT) spectra (Fig. 2f and g). The second prominent peak at ~2.59 Å in Os L<sub>3</sub>-edge EXAFS spectrum of 1 T-OsCoTe<sub>2</sub> can be attributed to Co–Os coordination at the first shell, which is similar to 2 H-OsCoTe<sub>2</sub> and different from that of Os–Te coordination. Of note, no significant peaks such as Os–Os (~2.68 Å) are detected on the longer backscattering paths (Fig. S7 and Table S1), indicating Os species in 1 T-OsCoTe<sub>2</sub> and 2 H-OsCoTe<sub>2</sub> exist in a single atomic state [26,31], which is consistent with XRD fitting results. Collectively, after the formation of 1 T-OsCoTe<sub>2</sub>, the number of electrons on Co atoms increases and the number of electrons on Os atoms decreases, and there may be transferred from Os to Co via Os–Te–Co electron bridging.

### 3.3. Photocatalytic CO<sub>2</sub>RR performance

The CO<sub>2</sub> photoreduction products were measured in MeCN aqueous solution (MeCN:H<sub>2</sub>O = 6:1, Fig. S8a) to evaluate CO<sub>2</sub>RR performance of the catalyst [13,32,33]. 50 mg of photocatalyst loading was adopted to improve C<sub>3</sub>H<sub>8</sub> selectivity (Fig. S8b). A similar photocatalyst dosage was often used in previous photocatalytic works. The gaseous and liquid

reduction products were analyzed and quantified via GC-MS and <sup>1</sup>H NMR spectroscopy, respectively (Fig. 3a and S9a–d). CO and CH<sub>4</sub> are mainly detected on 1 T-CoTe<sub>2</sub>, 2 H-OsTe<sub>2</sub>, and OsCo with yields of 33.74, 23.61, and 11.3 μmol g<sup>-1</sup> h<sup>-1</sup>, respectively (Fig. 3a). 1 T-OsCoTe<sub>2</sub> exhibits significant yields of C<sub>2</sub>H<sub>4</sub> (3.26 μmol g<sup>-1</sup> h<sup>-1</sup>) and C<sub>3</sub>H<sub>8</sub> (10.28 μmol g<sup>-1</sup> h<sup>-1</sup>), together with a small amount of CH<sub>4</sub> (1.78 μmol g<sup>-1</sup> h<sup>-1</sup>), in addition to CO (14.91 μmol g<sup>-1</sup> h<sup>-1</sup>) (Fig. 3b and c), exhibiting an exceptionally strong C–C coupling capability [34]. The C<sub>2</sub>H<sub>4</sub> and C<sub>3</sub>H<sub>8</sub> yields of 2 H-OsCoTe<sub>2</sub> are reduced to 2.27 and 7.72 μmol g<sup>-1</sup> h<sup>-1</sup>, indicating that the non-trivial TSSs of 1 T-OsCoTe<sub>2</sub> is conducive to the improvement of CO<sub>2</sub> activity through enhancing the adsorption of intermediates, promoting carrier mobility and reducing the activation energy of reactants [4,5]. Strikingly, an IQE<sub>cr</sub> of 1 T-OsCoTe<sub>2</sub> at the wavelength of 380, 400, 420, 440, 460, 480, 500, and 520 nm is 54.6%, 25.63 %, 10.84 %, 9.49 %, 7.12 %, 5.25 %, 2.80 %, and 1.27 %, respectively (Table S2) [35,36]. A high product-based selectivity of C<sub>3</sub>H<sub>8</sub> of 34.0 % is achieved (71.20 % of the electron-based selectivity), and that of total C<sub>2+</sub> hydrocarbons is as high as 44.8 % (84.7 % of the electron-based selectivity) (Fig. 3b) [37]. The catalytic activity of 1 T-OsCoTe<sub>2</sub> and 2 H-OsCoTe<sub>2</sub> is competitive with those of well-known photocatalysts under strict conditions (Table S3). Herein, we further tested the catalytic performance of 1 T-OsCoTe<sub>2</sub> and 2 H-OsCoTe<sub>2</sub> in pure H<sub>2</sub>O (with H<sub>2</sub>O as the electron donor), and the results shows that the generation rate of all carbon-based products decreased (Fig. S10a). Moreover, the C<sub>2+</sub> hydrocarbon selectivity of 1 T-OsCoTe<sub>2</sub> becomes lower in pure H<sub>2</sub>O (Fig. S10b). Interestingly, no C<sub>2+</sub> hydrocarbons of 2 H-OsCoTe<sub>2</sub> are detected in pure H<sub>2</sub>O, but more H<sub>2</sub> is produced with a formation rate of 3.84 μmol g<sup>-1</sup> h<sup>-1</sup> (10.27 % of the electron-based selectivity) (Fig. S8c and d). The improvement of the catalytic activity and selectivity may be attributed to the high solubility of CO<sub>2</sub> in MeCN, which significantly increases the local accessibility of CO<sub>2</sub>, thus enhancing the contact between 1 T-OsCoTe<sub>2</sub> and CO<sub>2</sub>, and promoting C–C coupling [34]. Enlightened via the analyses described above, the effective inhibition of CO generation and increased C<sub>2+</sub> hydrocarbons production on 1 T-OsCoTe<sub>2</sub> and 2 H-OsCoTe<sub>2</sub> confirm that the formation of C<sub>2+</sub> hydrocarbons are probably owing to the C–C coupling depletion of \*CO.

The gas production rate of 1 T-OsCoTe<sub>2</sub> under light irradiation was measured by cyclic tests, as shown in Fig. 3d and S11a–c, which is pivotal for evaluating the stability of the photocatalyst. The distinctive CO<sub>2</sub> photoreduction activity and high selectivity of C<sub>3</sub>H<sub>8</sub> and total C<sub>2+</sub> hydrocarbons are still well maintained after eight cycling tests of 40 h. This is further supported through XRD (S11d), XPS (Fig. S12) and XAFS (Fig. S13) spectra of 1 T-OsCoTe<sub>2</sub> after the stability tests. All the post-reaction characterizations indicate that 1 T-OsCoTe<sub>2</sub> has the excellent capability and stability to efficiently achieve the photoreduction of CO<sub>2</sub> to C<sub>2+</sub> hydrocarbons. Moreover, the isotropic experiment was further carried out by employing <sup>13</sup>CO<sub>2</sub> as a reactant to ascertain the carbon source of the products. <sup>13</sup>CO<sub>2</sub> isotope labeling experiment and the time profile of the relative abundance of <sup>13</sup>C labeled products confirm that the carbon source for CO(g) and other hydrocarbon products originates from the input CO<sub>2</sub>(g) (Fig. S9c and d) [38,39]. To explore the role of Te atoms in 1 T-OsCoTe<sub>2</sub>, OsCo was synthesized under the same conditions. In sharp contrast, OsCo is nearly photo-catalytically incapable toward CO<sub>2</sub>RR (Fig. 3b), confirming that Os–Te–Co electron bridging of 1 T-OsCoTe<sub>2</sub> promote photocatalytic activity. To elucidate the change in the valence states and the local structures surrounding Os and Co atoms, XAFS experiments further were performed in detail (Fig. S14). Compared with 1 T-OsCoTe<sub>2</sub>, both the valence states of Os and Co atoms shift to lower energy in OsCo. Co K-edge XANES curves show that the absorption edge of OsCo is between that of Co foil and 1 T-CoTe<sub>2</sub> (Fig. S14a), indicating that the valence state of Co atoms in OsCo is between 0 and +2, which may be caused by surface oxidation. Moreover, OsCo exhibits a lower intensity than 1 T-CoTe<sub>2</sub> (inset in Fig. S14a), implying that the introduction of Te atoms reduces the oxidation state of Co atoms in 1 T-CoTe<sub>2</sub> [40]. Meanwhile, EXAFS fitting shows that Co

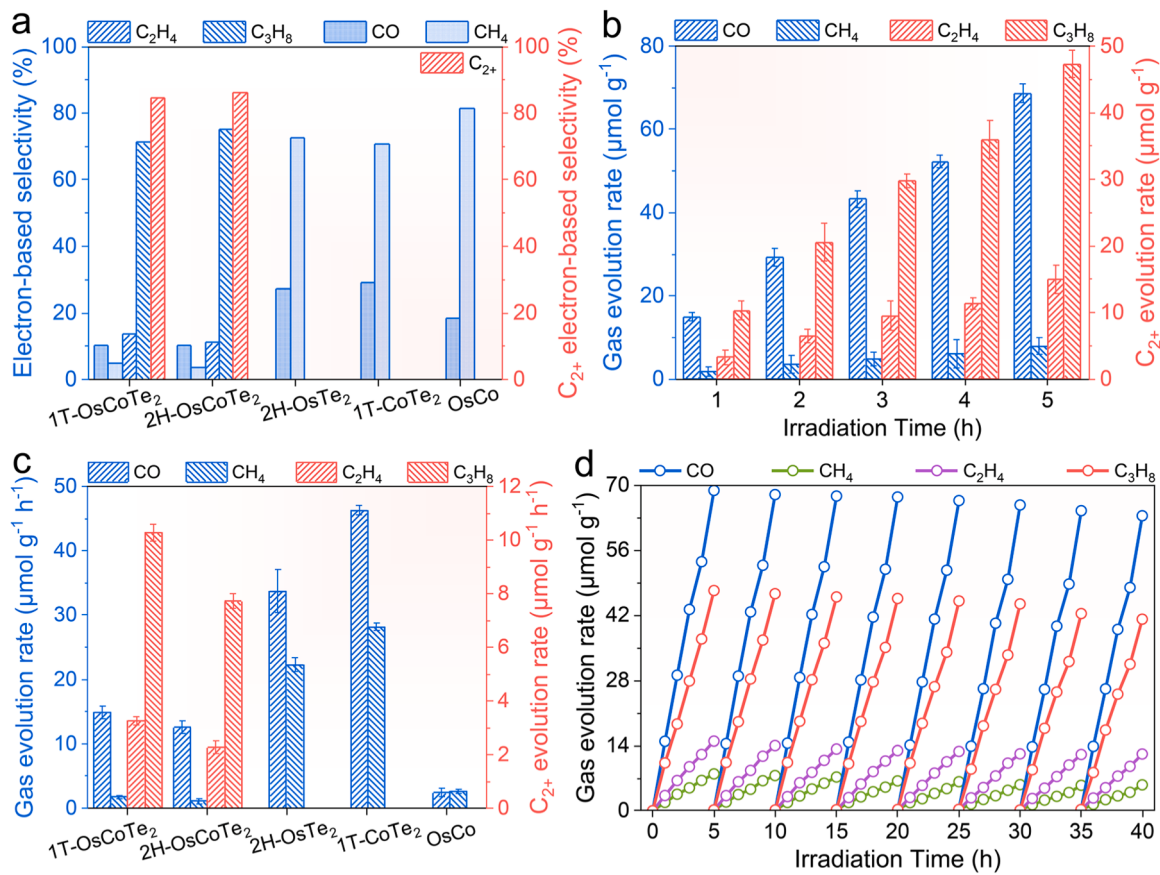


**Fig. 3.** (a) Electron-based selectivity on as-prepared samples in MeCN aqueous solution. (b) Photocatalytic product evolution as a function of light irradiation times on 1 T-OsCoTe<sub>2</sub> in MeCN aqueous solution. (c) Product formation rates on samples in MeCN aqueous solution. (d) Gas evolution amounts as a function of light irradiation time for 1 T-OsCoTe<sub>2</sub> over eight cycling tests in MeCN aqueous solution.

atoms in OsCo without the Te electron bridging is coordinated with Os atoms (Fig. S14b–f). As such, 1 T-OsCoTe<sub>2</sub> with Te electron bridging significantly accelerates photocatalytic CO<sub>2</sub> reduction to C<sub>2+</sub> hydrocarbons.

#### 3.4. Photoelectric performance analysis

The absorption edge of 1 T-OsCoTe<sub>2</sub> displays a blue shift compared with 2 H-OsCoTe<sub>2</sub> due to the non-trivial TSSs of 1 T-OsCoTe<sub>2</sub>, while the light absorption is enhanced after implantation of 1 T-CoTe<sub>2</sub> (Fig. S15a). Transient photocurrent measurements confirm the enhanced charge separation and migration efficiency of 1 T-OsCoTe<sub>2</sub>, ascribed to the non-trivial TSSs, which effectively shortens the charge transfer distance from body to surface and lowers charge recombination possibility (Fig. S15b). Theoretically, the fast charge carrier dynamics of 1 T-OsCoTe<sub>2</sub> is kinetically favorable for the multi-electron reactions of generating C<sub>2+</sub> hydrocarbons. Therefore, the photogenerated carrier separation efficiency was determined via steady-state PL, TRPL, and transient photocurrents. Dramatic PL quenching occurs on 1 T-OsCoTe<sub>2</sub> relative to OsCo, implying that the intrinsic radiative recombination of photo-generated carrier in 2 H-OsTe<sub>2</sub> has been substantially inhibited due to the promoted charge transfer through Os–Te–Co electron bridging (Fig. S15c). Moreover, the TRPL decay spectra recorded at the corresponding steady-state emission peaks illustrate that 1 T-OsCoTe<sub>2</sub> has a longer average lifetime ( $\tau_{avg}$ ) of charge carriers with respect to 1 T-CoTe<sub>2</sub> and 2 H-OsTe<sub>2</sub> (Fig. S15d and Table S5), meaning that there is efficient charge transfer in 1 T-OsCoTe<sub>2</sub> [41]. As shown in Figs. S15b, 1 T-OsCoTe<sub>2</sub> is favorable for charge separation from the enhancement of photocurrents. Peculiarly, the transient photocurrents density and PL density of 2 H-OsTe<sub>2</sub> are close to those of OsCo, illustrating that these

factors do not have much influence on the performance difference between 2 H-OsTe<sub>2</sub> and OsCo [42–44]. In contrast, the non-trivial TSSs of 1 T-OsCoTe<sub>2</sub> are better than those of 2 H-OsCoTe<sub>2</sub>, and thus should be the reason for the relatively higher performance of 1 T-OsCoTe<sub>2</sub>. Ultrafast femtosecond time-resolved transient absorption (fs-TA) spectroscopy provided evidence for the mechanism of photogenerated carrier transfer. As shown in Fig. 4a and b, TA spectra of 1 T-OsCoTe<sub>2</sub> and 2 H-OsCoTe<sub>2</sub> both demonstrate pronounced positive and negative absorption peaks at 440 and 493 nm, belonging to the excited state absorption (ESA) and ground state bleach (GSB), respectively [45,46], in which the GSB peak reflects the relaxation of the excited state. A redshift of GSB peak with pump-probe delay time can be observed in Fig. 4c and d, mainly due to the broad size distribution of Os atoms in 1 T-OsCoTe<sub>2</sub> and 2 H-OsCoTe<sub>2</sub>, where the smaller Os atoms have the larger band gaps and faster exciton annihilation [47,48]. To deeply analyze the dynamic behavior of charge carriers, GSB and ESA decay kinetics curves of both 1 T-OsCoTe<sub>2</sub> and 2 H-OsCoTe<sub>2</sub> are shown in Fig. 4e and f, respectively, which indicate that the kinetic decays of GSB and ESA are significantly suppressed on the probing time scale. The clear negative absorption bands attributed to the GSB peak signal can be observed, which implies charge carrier transfer between Os–Te–Co electron bridging [49], agreeing with the results of in-situ XPS and XAFS.

#### 3.5. Reaction mechanism analysis

To understand the mechanism of photocatalytic CO<sub>2</sub>RR at molecular level, the possible intermediates were performed by in-situ DRIFTS technique. In the spectra (Fig. 5a, b and Fig. S16a), the peaks at 1409/1432 cm<sup>-1</sup> belong to HCO<sub>3</sub><sup>-</sup> [50], while the peaks at 1276/1597 cm<sup>-1</sup> is assigned to bidentate carbonates (b-CO<sub>3</sub><sup>2-</sup>) [51,52]. In addition, a small

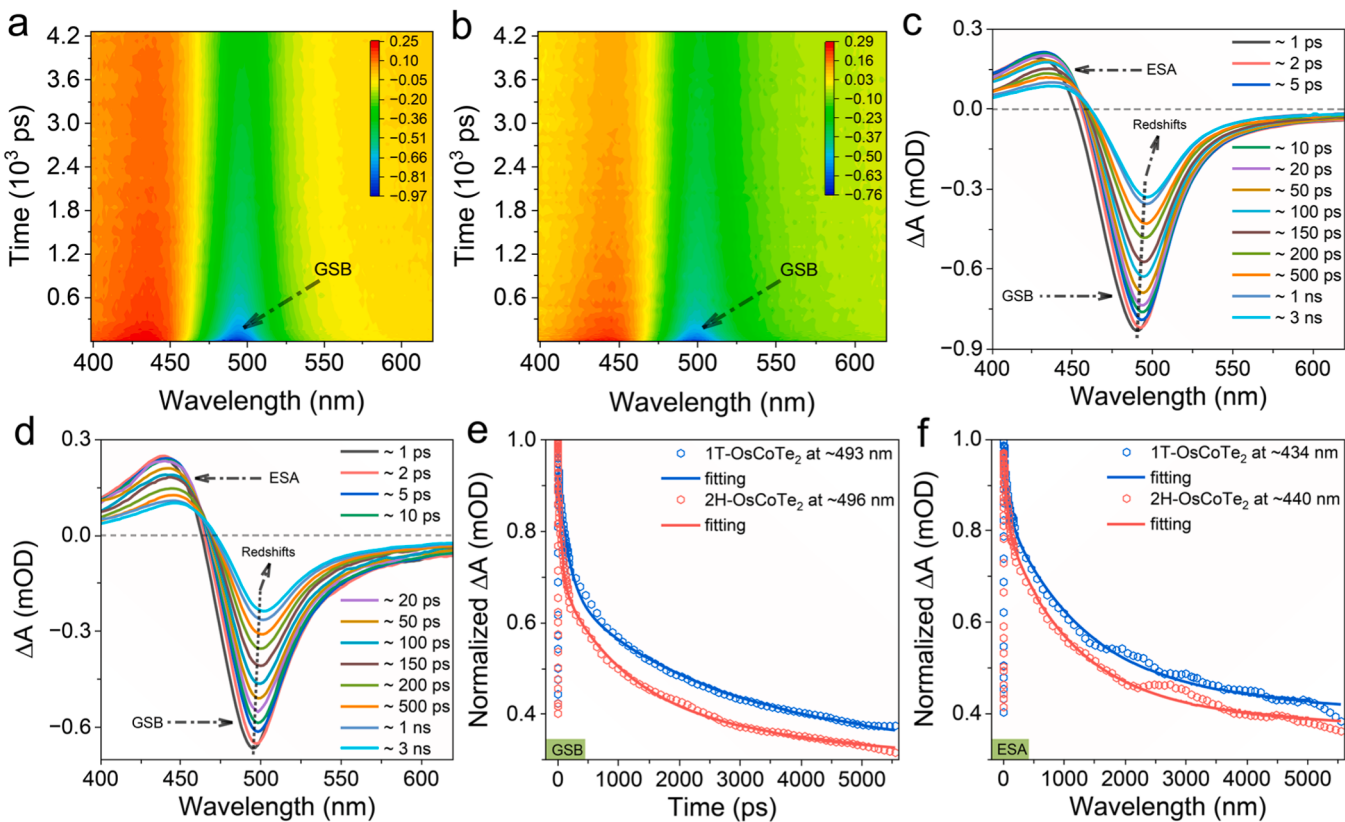


**Fig. 4.** 2D Pseudo-color images of (a) 1 T-OsCoTe<sub>2</sub> and (b) 2 H-OsCoTe<sub>2</sub> in ethanol solution after the excitation with a 310 nm laser pulse. The TA spectra of (c) 1 T-OsCoTe<sub>2</sub> and (d) 2 H-OsCoTe<sub>2</sub> at different delays time. (e) Comparison of decay kinetics and fitting lines for 1 T-OsCoTe<sub>2</sub> and 2 H-OsCoTe<sub>2</sub> taken through the GSB peaks at  $\sim 493$  and  $\sim 496$  nm, respectively. (f) Normalized decay kinetics and fitting lines for 1 T-OsCoTe<sub>2</sub> and 2 H-OsCoTe<sub>2</sub> taken through the ESA peaks at  $\sim 434$  and  $\sim 440$  nm, respectively.

amount of  ${}^*\text{CH}_3$  ( $1473\text{ cm}^{-1}$ ),  ${}^*\text{CO}_3$  ( $1510\text{ cm}^{-1}$ ),  $\text{CH}_3\text{O}^*$  ( $1127\text{ cm}^{-1}$ ) [37],  $\text{CHO}^*$  ( $1044\text{ cm}^{-1}$ ) and  $\text{CH}_2\text{O}^*$  ( $1711\text{ cm}^{-1}$ ) is observed, resulting from the intermediates to the production of  $\text{CH}_4$  ( $1352\text{ cm}^{-1}$ ) and  $\text{C}_3\text{H}_8$  [52,53]. The characteristic peaks of  ${}^*\text{COOH}$  at  $1563$  and  $1628\text{ cm}^{-1}$  appear as the most critical intermediates in the photoreduction of CO<sub>2</sub>-to-CO [13]. The increasing peak at  $2130\text{ cm}^{-1}$  may be derived from  ${}^*\text{CO}$ , a key intermediate in the formation of CO. The peaks at  $1980$  and  $2094\text{ cm}^{-1}$  are attributed to linear- and bridge-type CO adsorption at the Co sites, respectively (Fig. 5c). In addition, a new peak arising at  $2126\text{ cm}^{-1}$  over 1 T-OsCoTe<sub>2</sub> and 1 T-CoTe<sub>2</sub> is attributed to the linear CO adsorption on the non-trivial TSSs (as mentioned in the introduction), demonstrating the well-formed TSS of 1 T-CoTe<sub>2</sub> in the samples [5]. Of note, a broad peak at  $2039\text{ cm}^{-1}$  is observed, which belongs to bridge-type CO adsorption over 2 H-OsTe<sub>2</sub> [54], corresponding to the detection of carbonyl ( ${}^*\text{COOH}$ ,  ${}^*\text{CO}$ ,  ${}^*\text{CHO}$ , and  ${}^*\text{CHOCO}$ ) intermediates via in-situ DRIFTS [55,56]. In-situ electron paramagnetic resonance (ESR) spectroscopy was used to further detect free radicals produced by photoinduced activation of various reactants. As shown in Fig. 5d,  ${}^*\text{CH}_3$  is detected in addition to  ${}^*\text{OH}$  when  $\text{CH}_4$  is injected into an aqueous solution containing 1 T-OsCoTe<sub>2</sub> and 2 H-OsCoTe<sub>2</sub> under visible light illumination,  ${}^*\text{CH}_3$ , in addition to  ${}^*\text{OH}$ , are detected (Fig. S16b and c) [57,58]. In order to further understand CO<sub>2</sub>RR mechanism through elemental information, carbon and oxygen species on the surface of the material were also monitored by in-situ near ambient pressure XPS (NAP-XPS) measurements. As shown in Fig. 5e and S17, a peak of  $\text{CH}_4$  ( $287.0\text{ eV}$ ) is clearly detected in C 1 s XPS spectra (Fig. S17a). The C1s peaks of  ${}^*\text{CH}_x$ , C–O, and  ${}^*\text{COO}$  species occurring at  $285.4$ ,  $286.1$ , and  $289.2\text{ eV}$  increase with the time evolution upon visible light irradiation. Afterward, it is further verified that CO<sub>2</sub> was reduced to produce oxygen-containing compounds via collecting the O 1 s spectrum in NAP-XPS. The characteristic peaks of  ${}^*\text{OH}$  ( $531.1\text{ eV}$ ), C–O ( $531.9\text{ eV}$ ),

H<sub>2</sub>O ( $532.6\text{ eV}$ ), and C=O ( $533.3\text{ eV}$ ) could be resolved under visible light illumination (Fig. 5f). Interestingly, strong  ${}^*\text{CO}$  signals are observed with in-situ DRIFTS and NAP-XPS, but extremely little CO is detected on 1 T-OsCoTe<sub>2</sub> and 2 H-OsCoTe<sub>2</sub>. Indeed, Fig. 5d already reflects the relatively strong adsorption of CO on the Co active sites, allowing  ${}^*\text{CO}$  to couple to other intermediates before desorption [59, 60]. Taken together, the presence of  ${}^*\text{CH}_x$ , C–O, and  ${}^*\text{COO}$  was confirmed by a series of in-situ tests, indicating that the co-adsorption reaction of CO<sub>2</sub> and H<sub>2</sub>O on 1 T-OsCoTe<sub>2</sub> can generate a variety of surface carbonaceous intermediates (e.g., methyl and carbonyl) [54] and further C<sub>2+</sub> hydrocarbons. The experimental results have revealed the critical role of 1 T-OsCoTe<sub>2</sub> in CH<sub>4</sub>-to-CH<sub>4</sub>/C<sub>2</sub>H<sub>4</sub>/C<sub>3</sub>H<sub>8</sub> conversion. Fig. 6a and b illustrate the proposed reaction pathway. CO<sub>2</sub> prefers to be activated at Os sites in the presence of H<sup>+</sup> and form Os–OCH<sub>3</sub>. The  ${}^*\text{CH}_3$  can be gradually converted to Os–O through combining Te atoms from Os–Te unit and the hydrogenation via H<sup>+</sup> (Fig. 6b). Simultaneously, the C<sub>1</sub>–C<sub>1</sub> coupling between  ${}^*\text{CHO}$  and  ${}^*\text{CO}$  generates Co–CHOCO at Co–Te unit interface, and the further hydrolysis of Co–OCH<sub>2</sub>CO gives C<sub>2</sub>H<sub>4</sub> as a product. The Os sites are also active for Os–CO generation by directly oxidizing CO on Os–Te unit (Fig. 6a). However, the  ${}^*\text{CH}_3$  formed on Os–Te unit can hardly approach  ${}^*\text{CO}$  on Co–Te unit, so the surplus  ${}^*\text{CH}_3$  would evolve into CH<sub>4</sub> (Fig. 6b). Moreover, the formation of a five-membered ring between  ${}^*\text{CH}_2\text{OCOCO}$  and Co active sites significantly mitigates the accumulation of localized electrons and weakens inter- and intramolecular electrostatic repulsion (Fig. 6a). The electronic and non-trivial TSSs, as well geometrical effects of 1 T-OsCoTe<sub>2</sub> may have jointly stabilized critical  ${}^*\text{C}_{2+}$  intermediates and lowered their adsorption energy levels, thus facilitating C–C coupling [61–63].

To further probe the enhanced catalytic performance at the 1 T-OsCoTe<sub>2</sub>, the CO<sub>2</sub> activation process is first analyzed. From CO<sub>2</sub> adsorption isotherms, 1 T-OsCoTe<sub>2</sub> has a CO<sub>2</sub> adsorption capacity of

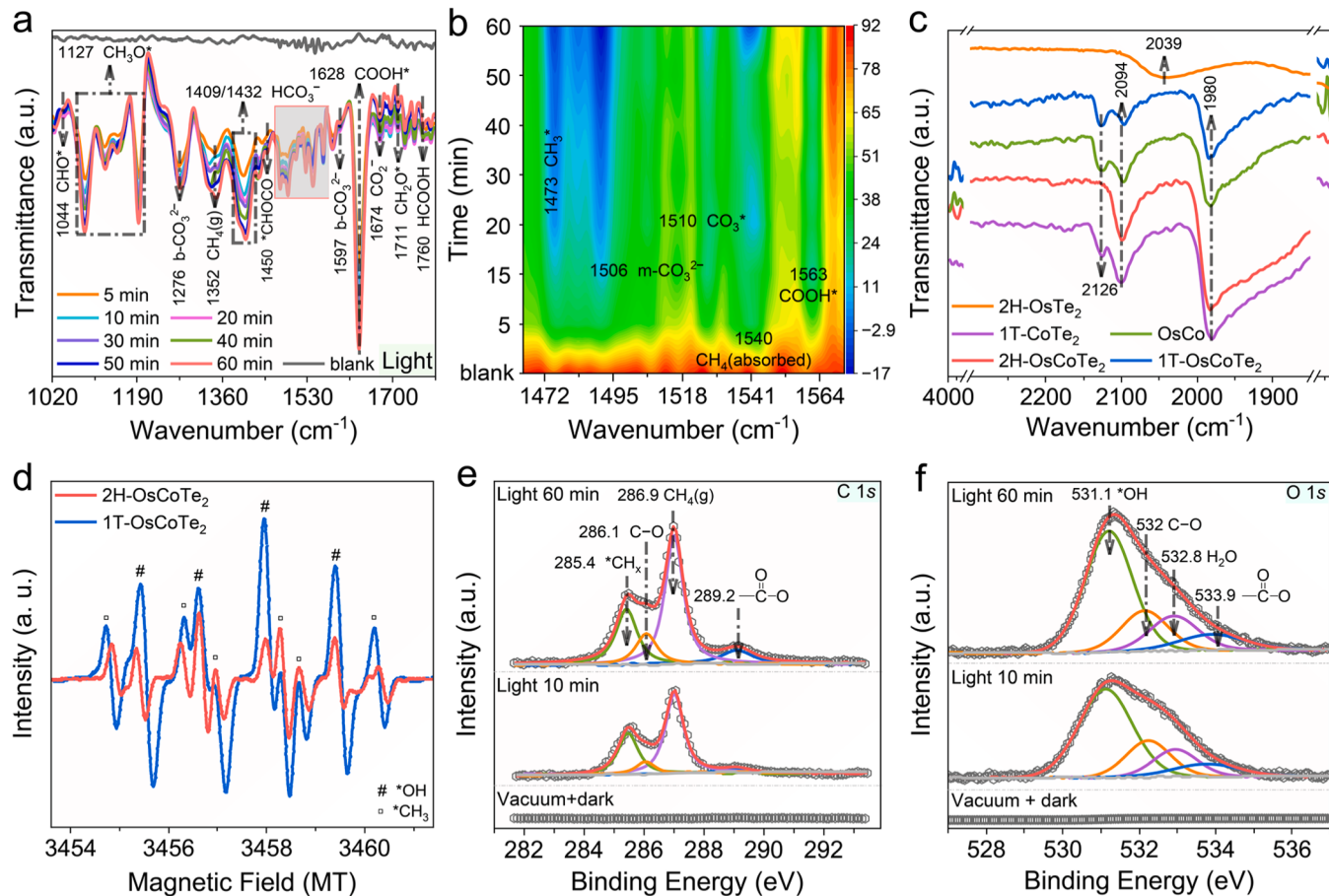


**Fig. 5.** (a,b) In-situ DRIFTS spectra for light-driven CO<sub>2</sub> conversion over 1 T-OsCoTe<sub>2</sub>. (c) CO adsorption DRIFTS spectra of samples. (d) In-situ ESR spectra of CO<sub>2</sub> + H<sub>2</sub>O mixture under light illumination at 298 K in the presence of DMPO over 1 T-OsCoTe<sub>2</sub> and 2 H-OsCoTe<sub>2</sub>. In-situ NAP-XPS results of high-resolution (e) C 1 s and (f) O 1 s spectra over 1 T-OsCoTe<sub>2</sub>.

49.69 cm<sup>3</sup> g<sup>-1</sup> under 1.0 atm at 298 K, which is about 1.31 times larger than that of 2 H-OsCoTe<sub>2</sub> (37.91 cm<sup>3</sup> g<sup>-1</sup>, Fig. S18a). CO<sub>2</sub> adsorption isotherms reveal that 1 T-OsCoTe<sub>2</sub> possesses the highest CO<sub>2</sub> uptake capacity, which is the prerequisite step for triggering subsequent CO<sub>2</sub>RR. Given that 1 T-OsCoTe<sub>2</sub> has a topological structure, this result suggests that the topological structure plays a crucial role in enhancing CO<sub>2</sub> adsorption capacity [13]. Benefiting from the microenvironment constructed via 1 T-CoTe<sub>2</sub>, the optimal 1-OsCoTe<sub>2</sub> exhibits a high CO<sub>2</sub> adsorption capacity, which is favorable for the CO<sub>2</sub>RR to C<sub>2</sub>H<sub>4</sub> and C<sub>3</sub>H<sub>8</sub>. As revealed by in-situ characterizations, \*COOH, \*CO, \*CHO, and \*CHOCO species are the key intermediates for conversion of CO<sub>2</sub>to-C<sub>2+</sub> hydrocarbons, which is closely related to the presence of coupling \*CO and Co sites in 1 T-OsCoTe<sub>2</sub>. In order to further elucidate the intrinsic reasons for the excellent catalytic activity of 1 T-OsCoTe<sub>2</sub>, to understand the nature of the photocatalyst active sites, and to analyze the reaction mechanism of coupling \*CO in the C<sub>3</sub>H<sub>8</sub> generation process, DFT calculations were carried out on the optimized 1 T-OsCoTe<sub>2</sub> and 2 H-OsCoTe<sub>2</sub> using the computational hydrogen electrode model (Fig. 6e, f, and S19) [34,64]. DFT calculation results show that \*CO is difficult to desorb on 1 T-OsCoTe<sub>2</sub>, rather than further hydrogenation or C–C coupling reaction, consistent with the result that CO is the major product on 1 T-OsCoTe<sub>2</sub> (Figs. 3c, 6c, and S20a). The absorbed CO<sub>2</sub> is firstly converted to \*CHO through \*COOH and \*CO on 1 T-OsCoTe<sub>2</sub> (Fig. S18b–f). Then, \*CHO at 1 T-OsCoTe<sub>2</sub> may couple with the CO diffusing from Co–Te unit to generate \*CHOCO with a free energy change of -0.783 eV [55,65]. The C<sub>1</sub>–C<sub>2</sub> coupling reaction (\*CH<sub>2</sub>OCOCO + \*CO → \*CH<sub>2</sub>OCOCO) is thermodynamically calculated to be a self-reversing proceeding exergonic reaction ( $\Delta G = -0.677 \text{ eV} < 0$ )

[66]. It is worth noting that, on 2 H-OsCoTe<sub>2</sub>, C<sub>1</sub>–C<sub>1</sub> coupling is challenging due to the large variation uphill energy changes, resulting in the hydrogenation of \*CO to CH<sub>4</sub> being preferred (Fig. S20b) [67,68]. Meanwhile, for 1 T-OsCoTe<sub>2</sub>, some of \*C<sub>2+</sub> species will continue hydrogenation through a series of proton-electron steps to form C<sub>2</sub>H<sub>4</sub>. The free energy changes of the rate-determining step (RDS) of C<sub>3</sub>H<sub>8</sub> formation path (Fig. 6c) and C<sub>2</sub>H<sub>4</sub> formation path (Fig. 6d) are calculated to be 1.623 and 1.98 e V, respectively, indicating that C<sub>3</sub>H<sub>8</sub> is easier to generate than C<sub>2</sub>H<sub>4</sub>. This is consistent with our experimental results of outperforming C<sub>3</sub>H<sub>8</sub> than C<sub>2</sub>H<sub>4</sub> yields on 1 T-OsCoTe<sub>2</sub>. The downslope energy change of C–C coupling on 1 T-OsCoTe<sub>2</sub> may be due to the low energy levels of \*CHOCO and \*CH<sub>2</sub>OCOCO (Fig. S20c–e). The above analysis shows that both C<sub>1</sub>–C<sub>1</sub> and C<sub>1</sub>–C<sub>2</sub> coupling reactions are favorable on 1 T-OsCoTe<sub>2</sub>, in contrast to 2 H-OsCoTe<sub>2</sub> and other reported catalysts with challenging C–C coupling.

#### 4. Conclusion

A simple solid-phase strategy constructs 1 T-OsCoTe<sub>2</sub> topological semimetal, meanwhile, the CO<sub>2</sub>RR properties and the function of Co and Os species in 1 T-OsCoTe<sub>2</sub> were systematically investigated. In-situ XPS and XAFS investigations reveal that Co and Os atoms coordinated with Te atoms enable an efficient site-to-site electron transfer to ensure the high efficiency of CO<sub>2</sub>RR. Experimental evidence suggests a high electron-based selectivity of 71.2 % for C<sub>3</sub>H<sub>8</sub> (product-based selectivity of 34.2 %) and 84.75 % for total C<sub>2+</sub> hydrocarbons (product-based selectivity of 44.79 %), as well as an IQE<sub>cr</sub> of 54.6 % at 380 nm. An in-depth mechanism study illustrates that the synergistic effect of

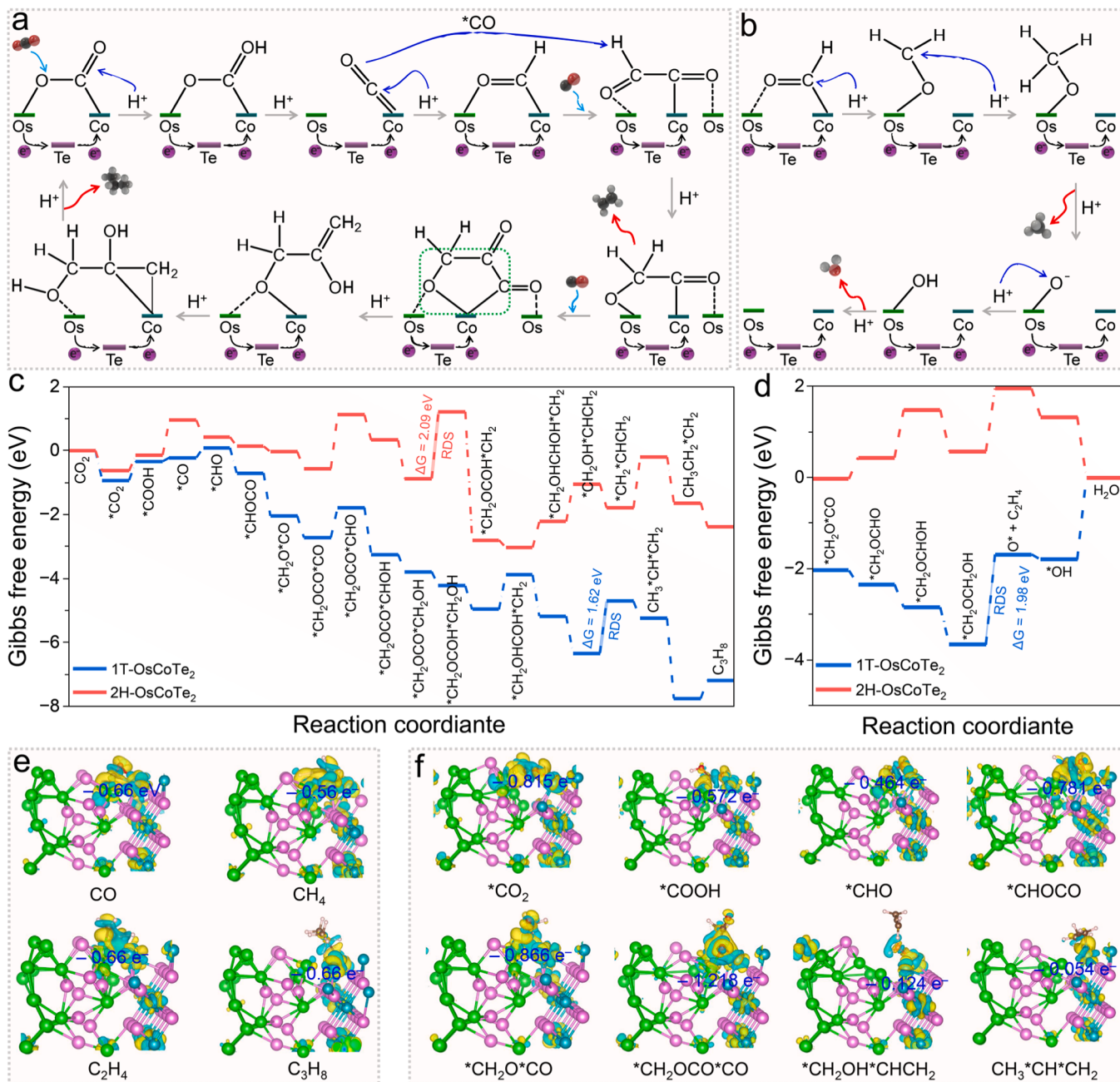


**Fig. 6.** Gibbs free energy diagrams of CO<sub>2</sub>RR on 1 T-OsCoTe<sub>2</sub> for (a) C<sub>2</sub>H<sub>4</sub> and C<sub>3</sub>H<sub>8</sub>, and (b) CH<sub>4</sub>, respectively. Gibbs free energy for steps in photocatalytic CO<sub>2</sub>-to-(c) C<sub>3</sub>H<sub>8</sub> and (d) C<sub>2</sub>H<sub>4</sub> conversion on 1 T-OsCoTe<sub>2</sub>. (e) Localized charge-density differences of CO, CH<sub>4</sub>, C<sub>2</sub>H<sub>4</sub>, and C<sub>3</sub>H<sub>8</sub> on 1 T-OsCoTe<sub>2</sub>. (f) Charge transfer diagrams of 1 T-OsCoTe<sub>2</sub> during CO<sub>2</sub>RR.

Os–Te–Co electron bridging can produce various surface carbonaceous intermediates, including \*CH<sub>3</sub> and \*CO, and further generate C<sub>2+</sub> products. In addition, the formation of a five-membered ring between \*CH<sub>2</sub>OOCOCO and Co–Te unit of 1 T-OsCoTe<sub>2</sub>, largely alleviating the local electron accumulation and weakens inter- and intramolecular electrostatic repulsion. The electronic and non-trivial TSSs, as well as geometrical effects of 1 T-OsCoTe<sub>2</sub>, may have combined to stabilize the critical \*C<sub>2+</sub> intermediates and lowered their adsorption energy levels, thus facilitating C–C coupling. This study provides insights into the photocatalytic performance of topological semimetallic catalysts and contributes to the design of new topological semimetal with excellent photoactivity. Meanwhile, an in-depth insight of the interfacial active sites at the atomic level is essential to analyze the reaction mechanisms and pathways.

#### CRediT authorship contribution statement

**Lingyong Zeng:** Methodology, Investigation. **Longfu Li:** Methodology, Investigation. **Chao Zhang:** Methodology, Investigation. **Kuan Li:** Methodology, Investigation. **Kai Yan:** Writing – review & editing, Project administration, Funding acquisition. **Kangwang Wang:** Writing – original draft, Methodology, Investigation, Formal analysis, Conceptualization. **Huixia Luo:** Writing – review & editing, Supervision, Project administration, Funding acquisition, Conceptualization. **Peifeng Yu:** Methodology, Investigation. **Mingjie Wu:** Methodology, Investigation. **Ying Liang:** Methodology, Investigation. **Hector F. Garces:** Writing – review & editing.

## Declaration of Competing Interest

The authors declare that they have no known competing financial interests or personal relationships that could have appeared to influence the work reported in this paper.

## Data Availability

Data will be made available on request.

## Acknowledgments

This work is supported by the Natural Science Foundation of China (11922415, 12274471, 22208331), Guangdong Basic and Applied Basic Research Foundation (2022A1515011168, 2019A1515011718, 2019A1515011337), 2024 Basic and Applied Basic Research Topic (Science and Technology Elite "Navigation" Project, 2024A04J6415), the Key Research & Development Program of Guangdong Province, China (2019B110209003).

## Appendix A. Supporting information

Supplementary data associated with this article can be found in the online version at [doi:10.1016/j.apcatb.2024.124058](https://doi.org/10.1016/j.apcatb.2024.124058).

## References

- [1] Y. Yang, S. Louisia, S. Yu, J. Jin, I. Roh, C. Chen, M.V. Fonseca Guzman, J. Feijoo, P.-C. Chen, H. Wang, C.J. Pollock, X. Huang, Y.-T. Shao, C. Wang, D.A. Muller, H. D. Abruna, P. Yang, Operando studies reveal active Cu nanograins for CO<sub>2</sub> electroreduction, *Nature* 614 (2023) 262–269.
- [2] C. Heide, Y. Kobayashi, D.R. Baykusheva, D. Jain, J.A. Sobota, M. Hashimoto, P. S. Kirchmann, S. Oh, T.F. Heinz, D.A. Reis, S. Ghimire, Probing topological phase transitions using high-harmonic generation, *Nat. Photonics* 16 (2022) 620–624.
- [3] G. Li, Y. Xu, Z. Song, Q. Yang, Y. Zhang, J. Liu, U. Gupta, V. Süß, Y. Sun, P. Sessi, S. S.P. Parkin, B.A. Bernevig, C. Felser, Obstructed surface states as the descriptor for predicting catalytic active sites in inorganic crystalline materials, *Adv. Mater.* 34 (2022) 2201328.
- [4] M.R. Scholz, J. Sánchez-Barriga, D. Marchenko, A. Varykhov, A. Volykhov, L. V. Yashina, O. Rader, Tolerance of topological surface states towards magnetic moments: Fe on Bi<sub>2</sub>Se<sub>3</sub>, *Phys. Rev. Lett.* 108 (2012) 256810.
- [5] H. Xie, T. Zhang, R. Xie, Z. Hou, X. Ji, Y. Pang, S. Chen, M.-M. Titirici, H. Weng, G. Chai, Facet engineering to regulate surface states of topological crystalline insulator bismuth rhombic dodecahedrons for highly energy efficient electrochemical CO<sub>2</sub> reduction, *Adv. Mater.* 33 (2021) 2008373.
- [6] H. Luo, P. Yu, G. Li, K. Yan, Topological quantum materials for energy conversion and storage, *Nat. Rev. Phys.* 4 (2022) 611–624.
- [7] Z. Hu, L. Zhang, A. Chakraborty, G. D'Olimpio, J. Fujii, A. Ge, Y. Zhou, C. Liu, A. Agarwal, I. Vobornik, D. Farias, C.-N. Kuo, C.S. Lue, A. Politano, S.-W. Wang, W. Hu, X. Chen, W. Lu, L. Wang, Terahertz nonlinear hall rectifiers based on spin-polarized topological electronic states in 1T-CoTe<sub>2</sub>, *Adv. Mater.* 35 (2023) 2209557.
- [8] T.-H. Lu, C.-J. Chen, M. Basu, C.-G. Ma, R.-S. Liu, The CoTe<sub>2</sub> nanostructure: an efficient and robust catalyst for hydrogen evolution, *Chem. Commun.* 51 (2015) 17012–17015.
- [9] Y. Liu, J. Sun, H. Huang, L. Bai, X. Zhao, B. Qu, L. Xiong, F. Bai, J. Tang, L. Jing, Improving CO<sub>2</sub> photoconversion with ionic liquid and Co single atoms, *Nat. Commun.* 14 (2023) 1457.
- [10] Z.Z. Fan, R.C. Luo, Y.X. Zhang, B. Zhang, P.L. Zhai, Y.T. Zhang, C. Wang, J.F. Gao, W. Zhou, L.C. Sun, J.G. Hou, Oxygen-bridged indium-nickel atomic pair as dual-metal active sites enabling synergistic electrocatalytic CO<sub>2</sub> reduction, *Angew. Chem. Int. Ed.* (2023).
- [11] H.-J. Liu, S. Zhang, Y.-M. Chai, B. Dong, Ligand modulation of active sites to promote cobalt-doped 1T-MoS<sub>2</sub> electrocatalytic hydrogen evolution in alkaline media, *Angew. Chem. Int. Ed.* 62 (2023) e202313845.
- [12] J. Wang, G. Wang, J. Zhang, Y. Wang, H. Wu, X. Zheng, J. Ding, X. Han, Y. Deng, W. Hu, Inversely tuning the CO<sub>2</sub> electroreduction and hydrogen evolution activity on metal oxide via heteroatom doping, *Angew. Chem. Int. Ed.* 60 (2021) 7602–7606.
- [13] Q. Zhang, S. Gao, Y. Guo, H. Wang, J. Wei, X. Su, H. Zhang, Z. Liu, J. Wang, Designing covalent organic frameworks with Co-O<sub>4</sub> atomic sites for efficient CO<sub>2</sub> photoreduction, *Nat. Commun.* 14 (2023) 1147.
- [14] G. Kresse, J. Hafner, Ab initio molecular dynamics for open-shell transition metals, *Phys. Rev. B* 48 (1993) 13115–13118.
- [15] W. Kohn, L.J. Sham, Self-consistent equations including exchange and correlation effects, *Phys. Rev.* 140 (1965) A1133–A1138.
- [16] R.J. Protheroe, T. Stanev, Limits on models of the ultrahigh energy cosmic rays based on topological defects [Phys. Rev. Lett. 77, 3708 (1996)], *Phys. Rev. Lett.* 78 (1997), 3420–3420.
- [17] S. Grimme, J. Antoni, S. Ehrlich, H. Krieg, A consistent and accurate ab initio parametrization of density functional dispersion correction (DFT-D) for the 94 elements H-Pu, *J. Chem. Phys.* 132 (2010) 154104.
- [18] S. Grimme, S. Ehrlich, L. Goerigk, Effect of the damping function in dispersion corrected density functional theory, *J. Comput. Chem.* 32 (2011) 1456–1465.
- [19] V.I. Anisimov, J. Zaanen, O.K. Andersen, Band theory and Mott insulators: Hubbard U instead of Stoner I, *Phys. Rev. B* 44 (1991) 943–954.
- [20] F. Li, X. Yue, Y. Liao, L. Qiao, K. Lv, Q. Xiang, Understanding the unique S-scheme charge migration in triazine/heptazine crystalline carbon nitride homojunction, *Nat. Commun.* 14 (2023) 3901.
- [21] K. Wang, Z. Huang, J. Wang, Synthesis of hierarchical tandem double Z-scheme heterojunctions for robust photocatalytic H<sub>2</sub> generation, *Chem. Eng. J.* 430 (2022) 132727.
- [22] M. Samanta, H. Tan, S. Laha, H.A. Vignolo-González, L. Grunenberg, S. Bette, V. Duppel, P. Schützendübe, A. Gouder, B. Yan, B.V. Lotsch, The weyl semimetals  $MiTe_4$  ( $M = Nb, Ta$ ) as efficient catalysts for dye-sensitized hydrogen evolution, *Adv. Energy Mater.* 13 (2023) 2300503.
- [23] X. Chia, Z. Sofer, J. Luxa, M. Pumera, Unconventionally layered CoTe<sub>2</sub> and NiTe<sub>2</sub> as electrocatalysts for hydrogen, *Evolv. Chem. Eur.* 13 (2017) 11719–11726.
- [24] J. Liu, Y. Shen, X. Gao, L. Lv, Y. Ma, S. Wu, X. Wang, Z. Zhou, GeN<sub>3</sub> monolayer: a promising 2D high-efficiency photo- hydrolytic catalyst with High carrier mobility transport anisotropy, *Appl. Catal. B: Environ.* 279 (2020) 119368.
- [25] M. Li, H. Zhu, Q. Yuan, T. Li, M. Wang, P. Zhang, Y. Zhao, D. Qin, W. Guo, B. Liu, X. Yang, Y. Liu, Y. Pan, Proximity electronic effect of Ni/Co diatomic sites for synergistic promotion of electrocatalytic oxygen reduction and hydrogen evolution, *Adv. Funct. Mater.* 33 (2023) 2210867.
- [26] J. Zhu, F. Xia, Y. Guo, R. Lu, L. Gong, D. Chen, P. Wang, L. Chen, J. Yu, J. Wu, S. Mu, Electron accumulation effect over osmium/erlichmane heterointerfaces for intensified pH-universal hydrogen evolution, *ACS Catal.* 12 (2022) 13312–13320.
- [27] R. Huang, Y. Wen, P. Miao, W. Shi, W. Niu, K. Sun, Y. Li, Y. Ji, B. Zhang, Constructing the oxygen diffusion paths for promoting the stability of acidic water oxidation catalysts, *Chem. Catal.* 3 (2023) 100667.
- [28] Y. Jiang, Y.-P. Deng, R. Liang, N. Chen, G. King, A. Yu, Z. Chen, Linker-compensated metal-organic framework with electron delocalized metal sites for bifunctional oxygen electrocatalysis, *J. Am. Chem. Soc.* 144 (2022) 4783–4791.
- [29] N. Wang, S. Ning, X. Yu, D. Chen, Z. Li, J. Xu, H. Meng, D. Zhao, L. Li, Q. Liu, B. Lu, S. Chen, Graphene composites with Ru-RuO<sub>2</sub> heterostructures: highly efficient Mott-Schottky-type electrocatalysts for pH-universal water splitting and flexible zinc-air batteries, *Appl. Catal. B: Environ.* 302 (2022) 120838.
- [30] L. Shi, X. Ren, Q. Wang, Y. Li, F. Ichihara, H. Zhang, Y. Izumi, L. Ren, W. Zhou, Y. Yang, J. Ye, Stabilizing atomically dispersed catalytic sites on tellurium nanosheets with strong metal-support interaction boosts photocatalysis, *Small* 16 (2020) 2002356.
- [31] Z. Jiang, X. Liu, X.-Z. Liu, S. Huang, Y. Liu, Z.-C. Yao, Y. Zhang, Q.-H. Zhang, L. Gu, L.-R. Zheng, L. Li, J. Zhang, Y. Fan, T. Tang, Z. Zhuang, J.-S. Hu, Interfacial assembly of binary atomic metal-Nx sites for high-performance energy devices, *Nat. Commun.* 14 (2023) 1822.
- [32] X.-Y. Dong, Y.-N. Si, Q.-Y. Wang, S. Wang, S.-Q. Zang, Integrating single atoms with different microenvironments into one porous organic polymer for efficient photocatalytic CO<sub>2</sub> reduction, *Adv. Mater.* 33 (2021) 2101568.
- [33] S. Yang, W. Hu, X. Zhang, P. He, B. Pattengale, C. Liu, M. Cendejas, I. Hermans, X. Zhang, J. Zhang, J. Huang, 2D covalent organic frameworks as intrinsic photocatalysts for visible light-driven CO<sub>2</sub> reduction, *J. Am. Chem. Soc.* 140 (2018) 14614–14618.
- [34] Y. Shen, C. Ren, L. Zheng, X. Xu, R. Long, W. Zhang, Y. Yang, Y. Zhang, Y. Yao, H. Chi, J. Wang, Q. Shen, Y. Xiong, Z. Zou, Y. Zhou, Room-temperature photosynthesis of propane from CO<sub>2</sub> with Cu single atoms on vacancy-rich TiO<sub>2</sub>, *Nat. Commun.* 14 (2023) 1117.
- [35] C. Ding, X. Lu, B. Tao, L. Yang, X. Xu, L. Tang, H. Chi, Y. Yang, D.M. Meira, L. Wang, X. Zhu, S. Li, Y. Zhou, Z. Zou, Interlayer spacing regulation by single-atom indium<sup>8+</sup>-N<sub>4</sub> on carbon nitride for boosting CO<sub>2</sub>/CO photo-conversion (n/a), *Adv. Funct. Mater.* (2023) 2302824.
- [36] K. Wang, Z. Hu, P. Yu, A.M. Balu, K. Li, L. Li, L. Zeng, C. Zhang, R. Luque, K. Yan, H. Luo, Understanding bridging sites and accelerating quantum efficiency for photocatalytic CO<sub>2</sub> reduction, *Nano-Micro Lett.* 16 (2023) 5.
- [37] J. Li, H. Huang, W. Xue, K. Sun, X. Song, C. Wu, L. Nie, Y. Li, C. Liu, Y. Pan, H.-L. Jiang, D. Mei, C. Zhong, Self-adaptive dual-metal-site pairs in metal-organic frameworks for selective CO<sub>2</sub> photoreduction to CH<sub>4</sub>, *Nat. Catal.* 4 (2021) 719–729.
- [38] H. Jiang, K.-i Katsumata, J. Hong, A. Yamaguchi, K. Nakata, C. Terashima, N. Matsushita, M. Miyauchi, A. Fujishima, Photocatalytic reduction of CO<sub>2</sub> on Cu<sub>2</sub>O-loaded Zn-Cr layered double hydroxides, *Appl. Catal. B: Environ.* 224 (2018) 783–790.
- [39] Q. Zhi, J. Zhou, W. Liu, L. Gong, W. Liu, H. Liu, K. Wang, J. Jiang, Covalent microporous polymer nanosheets for efficient photocatalytic CO<sub>2</sub> conversion with H<sub>2</sub>O, *Small* 18 (2022) 2201314.
- [40] C. Hu, Y. Zhang, A. Hu, Y. Wang, X. Wei, K. Shen, L. Chen, Y. Li, Near- and long-range electronic modulation of single metal sites to boost CO<sub>2</sub> electrocatalytic reduction, *Adv. Mater.* 35 (2023) 2209298.
- [41] W. Gao, X. Zhao, T. Zhang, X. Yu, Y. Ma, E.C. dos Santos, J. White, H. Liu, Y. Sang, Construction of diluted magnetic semiconductor to endow nonmagnetic semiconductor with spin-regulated photocatalytic performance, *Nano Energy* 110 (2023) 108381.

- [42] K. Wang, Z. Huang, X. Jin, D. Zhang, J. Wang, MOF-derived hollow porous  $ZnFe_2O_4/AgCl/Ag/C$  nanotubes with magnetic-dielectric synergy as high-performance photocatalysts for hydrogen evolution reaction, *Chem. Eng. J.* 422 (2021) 130140.
- [43] K. Wang, S. Zhan, H. Sun, D. Zhang, J. Wang, Hollow porous core-shell  $ZnFe_2O_4/AgCl$  nanocubes coated with EDTA and Ag nanoparticles for enhanced photocatalytic performances of visible-light-driven, *Chem. Eng. J.* 400 (2020) 125908.
- [44] R. Li, T. Takata, B. Zhang, C. Feng, Q. Wu, C. Cui, Z. Zhang, K. Domen, Y. Li, Criteria for efficient photocatalytic water splitting revealed by studying carrier dynamics in a model Al-doped  $SrTiO_3$  photocatalyst, *Angew. Chem. Int. Ed.* 62 (2023) e202313537.
- [45] H. Yu, Y. Wang, X. Zou, H. Han, H.K. Kim, Z. Yao, Z. Wang, Y. Li, H.M. Ng, W. Zhou, J. Zhang, S. Chen, X. Lu, K.S. Wong, Z. Zhu, H. Yan, H. Hu, Effects of halogenation of small-molecule and polymeric acceptors for efficient organic solar cells, *Adv. Funct. Mater.* 33 (2023) 2300712.
- [46] A.M. El-Zohry, B. Turedi, A. Alsalloum, P. Maity, O.M. Bakr, B.S. Ooi, O. F. Mohammed, Ultrafast transient infrared spectroscopy for probing trapping states in hybrid perovskite films, *Commun. Chem.* 5 (2022) 67.
- [47] J. Ran, H. Zhang, S. Fu, M. Jaroniec, J. Shan, B. Xia, Y. Qu, J. Qu, S. Chen, L. Song, J.M. Cairney, L. Jing, S.-Z. Qiao, NiPS<sub>3</sub> ultrathin nanosheets as versatile platform advancing highly active photocatalytic H<sub>2</sub> production, *Nat. Commun.* 13 (2022) 4600.
- [48] W. Huang, C. Su, C. Zhu, T. Bo, S. Zuo, W. Zhou, Y. Ren, Y. Zhang, J. Zhang, M. Rueping, Isolated electron trap-induced charge accumulation for efficient photocatalytic hydrogen production, *Angew. Chem.* 135 (2023) e202304634.
- [49] J. Kosco, S. Gonzalez-Carrero, C.T. Howells, T. Fei, Y. Dong, R. Sougrat, G. T. Harrison, Y. Firdaus, R. Sheelamantula, B. Purushothaman, F. Moruzzi, W. Xu, L. Zhao, A. Basu, S. De Wolf, T.D. Anthopoulos, J.R. Durrant, I. McCulloch, Generation of long-lived charges in organic semiconductor heterojunction nanoparticles for efficient photocatalytic hydrogen evolution, *Nat. Energy* 7 (2022) 340–351.
- [50] H. Yu, J. Li, Y. Zhang, S. Yang, K. Han, F. Dong, T. Ma, H. Huang, Three-in-one oxygen vacancies: whole visible-spectrum absorption, efficient charge separation, and surface site activation for robust CO<sub>2</sub> photoreduction, *Angew. Chem. Int. Ed.* 58 (2019) 3880–3884.
- [51] Q. Liu, C. Chen, K. Yuan, C.D. Sewell, Z. Zhang, X. Fang, Z. Lin, Robust route to highly porous graphitic carbon nitride microtubes with preferred adsorption ability via rational design of one-dimension supramolecular precursors for efficient photocatalytic CO<sub>2</sub> conversion, *Nano Energy* 77 (2020) 105104.
- [52] C. Ban, Y. Duan, Y. Wang, J. Ma, K. Wang, J. Meng, X. Liu, C. Wang, X. Han, G. Cao, L. Gan, X. Zhou, Isotype heterojunction-boosted CO<sub>2</sub> photoreduction to CO, *Nano-Micro Lett.* 14 (2022) 74.
- [53] S. Bai, W. Jing, G. He, C. Liao, F. Wang, Y. Liu, L. Guo, Near-infrared-responsive photocatalytic CO<sub>2</sub> conversion via in situ generated Co<sub>3</sub>O<sub>4</sub>/Cu<sub>2</sub>O, *ACS Nano* 17 (2023) 10976–10986.
- [54] W. Zhang, D. Xi, Y. Chen, A. Chen, Y. Jiang, H. Liu, Z. Zhou, H. Zhang, Z. Liu, R. Long, Y. Xiong, Light-driven flow synthesis of acetic acid from methane with chemical looping, *Nat. Commun.* 14 (2023) 3047.
- [55] X.-F. Qiu, H.-L. Zhu, J.-R. Huang, P.-Q. Liao, X.-M. Chen, Highly selective CO<sub>2</sub> electroreduction to C<sub>2</sub>H<sub>4</sub> using a metal-organic framework with dual active sites, *J. Am. Chem. Soc.* 143 (2021) 7242–7246.
- [56] J. Liang, H. Zhang, Q. Song, Z. Liu, J. Xia, B. Yan, X. Meng, Z. Jiang, X.W. Lou, C.-S. Lee, Modulating charge separation of oxygen-doped boron nitride with isolated Co atoms for enhancing CO<sub>2</sub>-to-CO photoreduction, *Adv. Mater.* 36 (2024) 2303287.
- [57] S. Zhang, C. Huang, Z. Shao, H. Zhou, J. Chen, L. Li, J. Lu, X. Liu, H. Luo, L. Xia, H. Wang, Y. Sun, Revealing and regulating the complex reaction mechanism of CO<sub>2</sub> hydrogenation to higher alcohols on multifunctional tandem catalysts, *ACS Catal.* 13 (2023) 3055–3065.
- [58] H. Xu, D. Rebollar, H. He, L. Chong, Y. Liu, C. Liu, C.-J. Sun, T. Li, J.V. Muntean, R. E. Winans, D.-J. Liu, T. Xu, Highly selective electrocatalytic CO<sub>2</sub> reduction to ethanol by metallic clusters dynamically formed from atomically dispersed copper, *Nat. Energy* 5 (2020) 623–632.
- [59] J. Chen, J. Zhong, Y. Wu, W. Hu, P. Qu, X. Xiao, G. Zhang, X. Liu, Y. Jiao, L. Zhong, Y. Chen, Particle size effects in stoichiometric methane combustion: structure-activity relationship of Pd catalyst supported on gamma-alumina, *ACS Catal.* 10 (2020) 10339–10349.
- [60] T. Cheng, H. Xiao, W.A. Goddard III, Reaction mechanisms for the electrochemical reduction of CO<sub>2</sub> to CO and formate on the Cu(100) surface at 298 K from quantum mechanics free energy calculations with explicit water, *J. Am. Chem. Soc.* 138 (2016) 13802–13805.
- [61] J. Zhu, W. Shao, X. Li, X. Jiao, J. Zhu, Y. Sun, Y. Xie, Asymmetric triple-atom sites confined in ternary oxide enabling selective CO<sub>2</sub> photothermal reduction to acetate, *J. Am. Chem. Soc.* 143 (2021) 18233–18241.
- [62] W. Wang, C. Deng, S. Xie, Y. Li, W. Zhang, H. Sheng, C. Chen, J. Zhao, Photocatalytic C-C coupling from carbon dioxide reduction on copper oxide with mixed-valence copper(I)/copper(II), *J. Am. Chem. Soc.* 143 (2021) 2984–2993.
- [63] M. Esmaeilirad, Z. Jiang, A.M. Harzandi, A. Kondori, M. Tamadoni Saray, C. U. Segre, R. Shahbazian-Yassar, A.M. Rappe, M. Asadi, Imidazolium-functionalized Mo<sub>3</sub>P nanoparticles with an ionomer coating for electrocatalytic reduction of CO<sub>2</sub> to propane, *Nat. Energy* 8 (2023) 891–900.
- [64] X. Liu, J. Xiao, H. Peng, X. Hong, K. Chan, J.K. Nørskov, Understanding trends in electrochemical carbon dioxide reduction rates, *Nat. Commun.* 8 (2017) 15438.
- [65] A.J. Garza, A.T. Bell, M. Head-Gordon, Mechanism of CO<sub>2</sub> reduction at copper surfaces: pathways to C<sub>2</sub> products, *ACS Catal.* 8 (2018) 1490–1499.
- [66] C. Du, J.P. Mills, A.G. Yohannes, W. Wei, L. Wang, S. Lu, J.-X. Lian, M. Wang, T. Guo, X. Wang, H. Zhou, C.-J. Sun, J.Z. Wen, B. Kendall, M. Couillard, H. Guo, Z. Tan, S. Siahrostami, Y.A. Wu, Cascade electrocatalysis via AgCu single-atom alloy and Ag nanoparticles in CO<sub>2</sub> electroreduction toward multicarbon products, *Nat. Commun.* 14 (2023) 6142.
- [67] X. Li, Y. Sun, J. Xu, Y. Shao, J. Wu, X. Xu, Y. Pan, H. Ju, J. Zhu, Y. Xie, Selective visible-light-driven photocatalytic CO<sub>2</sub> reduction to CH<sub>4</sub> mediated by atomically thin CuIn<sub>5</sub>S<sub>8</sub> layers, *Nat. Energy* 4 (2019) 690–699.
- [68] Z.-W. Wang, Q. Wan, Y.-Z. Shi, H. Wang, Y.-Y. Kang, S.-Y. Zhu, S. Lin, L. Wu, Selective photocatalytic reduction CO<sub>2</sub> to CH<sub>4</sub> on ultrathin TiO<sub>2</sub> nanosheet via coordination activation, *Appl. Catal. B: Environ.* 288 (2021) 120000.